Heterogeneous Catalysis

International Edition: DOI: 10.1002/anie.201606046
German Edition: DOI: 10.1002/ange.201606046

Imaging of Oxygen Diffusion in Individual Platinum/$Ce_2Zr_2O_x$ Catalyst Particles During Oxygen Storage and Release

Hirosuke Matsui, Nozomu Ishiguro, Kaori Enomoto, Oki Sekizawa, Tomoya Uruga, and Mizuki Tada**

Abstract: *The spatial distribution of Ce^{3+} and Ce^{4+} in each particle of $Ce_2Zr_2O_x$ in a three-way conversion catalyst system was successfully imaged during an oxygen storage/release cycle by scanning X-ray absorption fine structure (XAFS) using hard X-ray nanobeams. For the first time, nano-XAFS imaging visualized and identified the modes of non-uniform oxygen diffusion from the interface of Pt catalyst and $Ce_2Zr_2O_x$ support and the active parts in individual catalyst particles.*

Heterogeneous solid catalysts are utilized for various chemical processes and are intrinsically non-uniform with respect to structure. Solid catalysts are typically in powder form, which is an assembly of non-uniform particles with different structural components (morphology, surface structure, domain boundary, oxygen content, and so forth).[1] In practice, the reactivity of a solid catalyst is evaluated based on the average of these structural components, and as a result it remains difficult to understand the real variation of the active parts in a heterogeneous catalyst. To solve this problem, spatially resolved imaging of chemical states in an individual catalyst particle is highly sought to reveal the active parts and non-uniform reaction modes at the nanoscale.

Ce is a key element for the oxygen storage/release function in a three-way catalyst system for clean-up of gaseous automobile exhaust; a redox process between Ce^{3+} and Ce^{4+} controls oxygen content in these catalyst systems.[2] However, it is well-known that only Ce species with extensive surface defects can contribute to the redox process in pure ceria, which offers insufficient oxygen storage/release capacity. $Ce_2Zr_2O_x$ (CZ; $x = 7$–8) solid–solution crystal contains an ordered arrangement of Ce and Zr atoms and exhibits excellent oxygen storage/release properties.[3] Almost 90% of the Ce atoms in CZ bulk can participate in the redox process between oxidized κ-phase $Ce_2Zr_2O_8$ and reduced pyrochlore $Ce_2Zr_2O_7$. Stoichiometric changes in the Ce valence states in response to oxygen diffusion in CZ bulk offers remarkable catalytic performance, such as automobile exhaust-gas cleaning over Pt/CZ[4,5] and methane steam-reforming over Ni/CZ.[6]

Recently, there have been remarkable developments in X-ray imaging techniques[7] and XAFS imaging is promising for revealing non-uniform behavior in practical materials.[8] We previously reported the spatial distribution of Ce oxidation states in individual particles of Pt/CZ catalysts by spatially resolved scanning nano-XAFS.[9] Ex situ nano-XAFS analysis revealed differences in Ce oxidation states in individual Pt/CZ particles with different oxygen contents. However, the size of Pt nanoparticles on CZ surfaces (< 10 nm) was much smaller than the size of probe X-ray beams (> 100 nm), and details regarding oxygen diffusion from the interface of the Pt catalyst into the CZ bulk were not reported because of a lack of spatial information about the Pt nanoparticles on CZ support.

Herein, we report the imaging of oxygen diffusion in individual CZ particles in contact with micron-sized catalytically active Pt particle for a reversible oxygen storage/release cycle. Using 100 nm sized hard X-ray beams, we investigated the nano-XAFS imaging for several CZ particles with different locations of attached Pt particles, as well as the two-dimensional images of Ce oxidation states. Nano-XAFS images showed the mode of oxygen diffusion, which was recorded during oxygen storage/release processes. For the first time, the present study has enabled clear visualization of Ce valence states in the CZ particles, which is changed at the interface of the Pt catalyst by oxygen diffusion.

Micron-sized Pt particles (Alfa Aesar, 0.2–1.6 μm) and CZ particles (0.2–2.0 μm) were dispersed on a SiN membrane by an impregnation method. SEM analysis measured by BEI mode showed significant contrast between Pt (bright image) and CZ particles (dark image; Figure 1a; Supporting Information, Figure S1). We selected several isolated CZ particles with different Pt locations on the SiN membrane: 1) **Particle 1**, a CZ particle with Pt attached to the side of the particle; 2) **Particle 2**, a CZ particle with Pt attached to the edge corner of the particle; and 3) **Particle 3**, a CZ particle without Pt (Figure 1a; Supporting Information, Figure S2). Ce $L\alpha$ and Pt $L\alpha$ XRF mappings using nano-X-ray beams clearly showed the locations and morphologies of both Pt and CZ particles in the selected assemblies, as shown in Figure 1b and 1c.

CZ and Pt/CZ exhibited sufficient oxygen storage/release performances: 86% of stoichiometric oxygen was contributed

[*] Dr. H. Matsui, K. Enomoto, Prof. Dr. M. Tada
Department of Chemistry, Graduate School of Science & Research Center for Materials Science (RCMS) & Integrated Research Consortium on Chemical Sciences (IRCCS), Nagoya University
Furo, Chikusa, Nagoya, Aichi 464-8602 (Japan)
E-mail: mtada@chem.nagoya-u.ac.jp
Dr. N. Ishiguro, Prof. Dr. M. Tada
RIKEN SPring-8 Center
Koto, Sayo, Hyogo 679-5198 (Japan)
Dr. O. Sekizawa, Prof. Dr. T. Uruga
Innovation Research Center for Fuel Cells, The University of Electro-Communications, Tokyo (Japan)
Prof. Dr. T. Uruga
Japan Synchrotron Radiation Research Center, Hyogo (Japan)

Supporting information for this article can be found under: http://dx.doi.org/10.1002/anie.201606046.

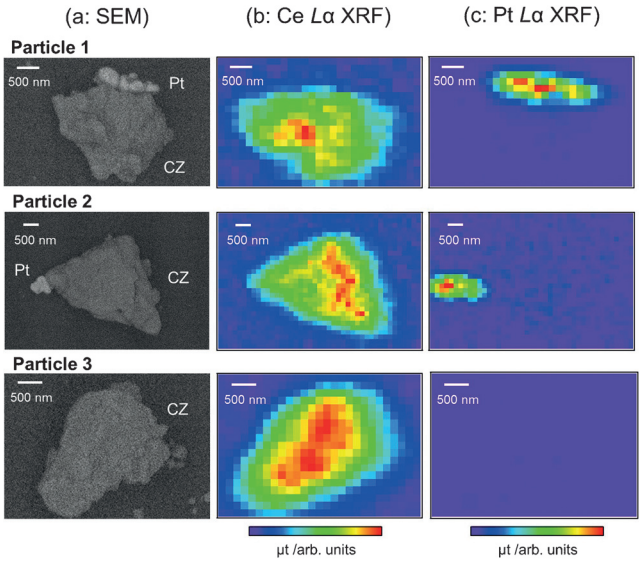

Figure 1. A) SEM images (BEI mode), B) Ce $L\alpha$, and C) Pt $L\alpha$ XRF mappings of three CZ particles (**1**–**3**) on a SiN membrane.

by temperature-programmed reduction and oxidation (TPR and TPO; Supporting Information, Figure S3). It was found that the attachment of Pt significantly changed the temperature of oxygen release by reduction, while the temperature of oxygen storage was not affected by the attachment of Pt. At 573 K, the phase transition between κ-phase $Ce_2Zr_2O_8$ and pyrochlore $Ce_2Zr_2O_7$ completed reversibly, as characterized by X-ray diffraction and Raman spectra. When $Ce_2Zr_2O_8$ was reduced to $Ce_2Zr_2O_7$ at 573 K, the (440) diffraction peak shifted from 48.8 to 47.7°; the Raman peaks attributed to Zr–O bonds in $Ce_2Zr_2O_8$[10] changed to the broad peaks of $Ce_2Zr_2O_7$[11] (Supporting Information, Figure S4).

We measured X-ray diffraction of CZ particles dispersed on the SiN membrane and investigated the variation of oxygen storage/release reactivity in these CZ particles on the membrane. The (440) peak at 48.8° in a fully oxidized sample (Supporting Information, Figure S5(1)) shifted to around 48.0° and was significantly broadened by the reduction at 423 K (Supporting Information, Figure S5(2)), indicating that most of the supported CZ particles had reacted but that there was significant variation in the local reactivity at this reaction temperature. A similar shift in the (440) diffraction peak was also observed in the oxygen storage process at 423 K (Supporting Information, Figure S5(4)), while broadening of the peak was relatively small compared to the oxygen release process. Further reduction and oxidation at 573 K completed both oxygen release and storage, resulting in the formation of sharp peaks of pyrochlore $Ce_2Zr_2O_7$ and κ-phase $Ce_2Zr_2O_8$, respectively (Supporting Information, Figures S5(3) and S5(5)). These results suggest that the supported CZ particles macroscopically followed reversible oxygen storage/release behavior under identical reaction conditions. However, there were significant differences in the reactivity of the oxygen storage/release on each CZ particle, and the reactions at 423 K show intermediate phases in the mode of oxygen diffusion for the oxygen storage/release inside the CZ particles.

Hence, we investigated the nano-XAFS analysis of the three CZ particles for the oxygen storage/release processes at 423 and 573 K. Scanning nano-XAFS spectra were measured at the BL36XU and BL39XU undulator beamlines at SPring-8 (Supporting Information, Figure S6). Monochromatized X-rays around 6 keV were focused by Kirkpatrick–Baez mirrors to a size of 409 (h) × 154 (v) nm to irradiate a sample enclosed in an XAFS cell mounted on an encoded-feedback translation stage. Two-dimensional nano-X-ray fluorescent images of the sample were obtained with a step size of 150 nm in the energy range of the Ce L_{III}-edge (Supporting Information, Figure S7), for which the XANES spectrum is highly sensitive to valence changes between Ce^{3+} and Ce^{4+}. The ratio of peak intensities at 5.7302 keV (assigned to the $2p \rightarrow 4f^15d^1$ (B_0) mode transition of Ce^{3+}), and 5.7344 and 5.7410 keV (assigned to the $2p \rightarrow 4f^15d^1L$ (B_1) mode and $4f^05d^1$ (C) mode transitions of Ce^{4+}), is relative to the Ce valence states between Ce^{3+} and Ce^{4+} (Supporting Information, Figure S8).[12] Although three-dimensional structural information is reduced to two-dimensional projection by nano-XAFS, the intensity ratio of these peaks provided the two-dimensional mapping of Ce^{3+}/Ce^{4+} distribution in each particle for the oxygen storage/release, as shown in Figure 2.[9]

In the case of **Particle 1**, in which the Pt was attached to the side of the CZ particle, the Ce valence state changed smoothly during both oxygen storage and release processes at 573 K (Figure 2(b-1) and (d-1)). The non-uniform distribution of unreacted parts inside the CZ particle was observed with oxygen storage at 423 K, but it was irrelevant to the attachment position of the Pt catalyst (Figure 2(a-1)). Such non-uniform distribution of unreacted parts was not observed in the oxygen release process at 423 K on **Particle 1** (Figure 2(c-1)).

It should be noted that **Particle 2**, in which the Pt particle was attached to the edge corner of the CZ particle, exhibited an isotropic gradient in the oxidation state of Ce^{3+} and Ce^{4+} with respect to the center of Pt particles, suggesting that Pt catalyst played a crucial role in the oxygen release. For oxygen storage at 423 K, a significant contrast marked in purple to red was observed across the entire area of the CZ particle (Figure 2(a-2)). This was observed to be independent of the position of the attached Pt, indicating that oxygen storage occurred in domains of the CZ particle without the contribution of the Pt catalyst. We performed the deconvolution of the Ce L_{III}-edge nano-XANES spectra at the representative positions **A**–**E** in **Particle 2** with respect to the XANES spectra of pyrochlore $Ce_2Zr_2O_7$ (Ce^{3+}; blue dashed line) and κ-phase $Ce_2Zr_2O_8$ (Ce^{4+}; red dashed line) presented in Figure 2(a-2-XANES). The nano-XANES spectra at positions **A**–**E** were significantly different, reflecting the variations in the valence states of Ce species, and agreed with the 2D mapping of the Ce oxidation states in Figure 2(a-2). After oxidation at 573 K, all Ce species in **Particle 2** were fully converted to Ce^{4+} (Figure 2(b-2)).

In contrast, it was found that oxygen release was remarkably controlled by the Pt catalyst. The oxygen release at 423 K started from the area where the Pt was attached, as shown in Figure 2(c-2). The Ce L_{III}-edge nano-XANES

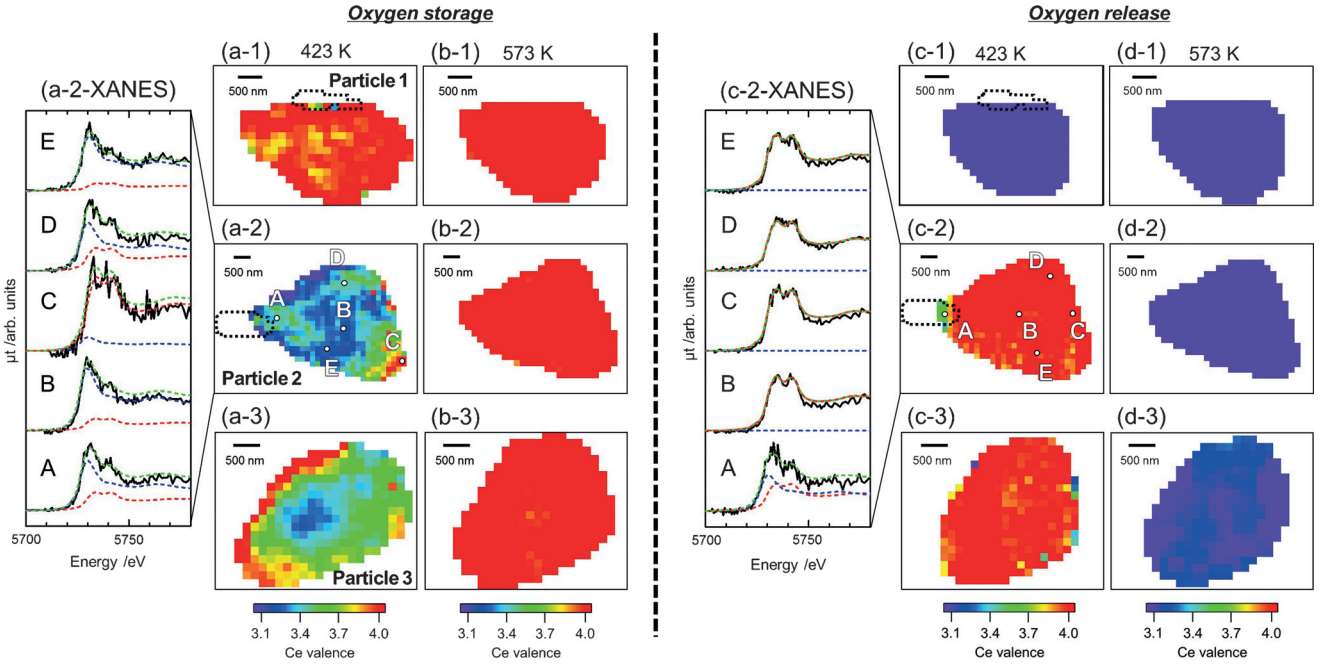

Figure 2. a)–d) The 2D mappings of Ce valence states of **Particles 1–3** after oxygen storage and release processes at 423 and 573 K. Black dotted lines indicate the position of Pt particles. a/c-2-XANES) Ce L_{III}-edge nano-XANES spectra (black lines) shown at representative points **A–E** in **Particle 2**. Blue, red, and green dashed lines present fitted spectra of Ce^{3+}, Ce^{4+}, and their summation. Oxygen storage and release were processed with a flow of O_2 or 10% H_2/N_2 at 1000 mL min^{-1} for 1 h.

spectra suggest that 50% of the Ce at position **A** (close to the Pt catalyst) was converted to Ce^{3+}, while positions **B–E** (far from the Pt catalyst) did not react at all at this stage (Figure 2(c-2-XANES)). These results clearly suggest that the initiation of oxygen release locally proceeds from the attached Pt catalyst and oxygen diffusion spreads into the CZ bulk. The scanning nano-XAFS imaging evidenced the significance of the interface between the Pt catalyst and the CZ particle as a preferential oxygen release site, though the detail of the interface structure is not clear at the moment. Nevertheless, at 573 K oxygen release completed throughout the entire area of **Particle 2** (Figure 2(d-2)).

In the case of **Particle 3** without Pt, oxygen storage proceeded independently of the absence of Pt, and oxygen diffusion from the CZ surface into the bulk was observed (Figure 2(a-3) and (b-3)). The different modes of oxygen diffusion in **Particles 2** and **3** are thought to be caused by differences in the non-uniform domain structures in the CZ particles. In contrast, oxygen release was almost inactive at 423 K (Figure 2(c-3)) and was not completed at 573 K because blue parts still remained in Figure 2(d-3). These results suggest that the absence of Pt strongly affected the reaction rate of oxygen release, in agreement with the results of TPR. Nano-XANES spectra of **Particles 1** and **3** agreed with the results of the 2D mapping of the Ce oxidation states (Supporting Information, Figures S9 and S10). Similar trends were observed for other particles (Supporting Information, Figure S11).

Oxygen diffusion is the key process of the oxygen storage/release function and proceeds by changing the Ce oxidation states in CZ. In the oxygen storage process, the activation of O_2 is thought to proceed at defect sites on the surface of the pyrochlore structure parts of the CZ support, and the subsequent oxygen diffusion spreads into the CZ bulk. The nano-XAFS imaging visualized the non-uniform domains forming in the oxygen diffusion process, even in the CZ crystal particles with a single-phase XRD pattern. The non-uniform domains are thought to provide a different distribution of surface defect sites, resulting in the non-uniform reaction in individual particles observed in Figure 2a.

In contrast, oxygen release by reduction with H_2 initiates at the Pt catalysts on the surface of κ-phase CZ. In situ time-resolved XAFS analysis of Pt/CZ revealed the activation energy of oxygen release as 43 kJ mol^{-1} at both the Ce L_{III}- and Zr K-edges.[5] The reaction mechanism of oxygen release on Pt/ceria has been discussed, and it was reported that morphology of ceria support was highly affected by oxygen transfer on nanostructured ceria in close contact with Pt.[13] If activated hydrogen formed on the Pt catalyst transfers by spillover to the entire surface of CZ, color changes in the mapping of Ce oxidation states in Figure 2(c-2) would be independent of the position of Pt. The anisotropic results in Figure 2(c-2) imply that activated hydrogen formed on the Pt catalyst reacts with oxygen at the interface of Pt and κ-phase CZ, and oxygen diffusion proceeds inside the CZ particle to the interface. The CZ support itself does not smoothly promote the reduction process, resulting in incomplete oxygen release in the CZ bulk, as observed in Figure 2(c/d-3).

Practical three-way conversion catalysts consist of nano-sized Pt particles on the surface of a Ce-based support.

Although the support material has intrinsic structural heterogeneity, it is thought that nanosized Pt catalysts spread on the support surface could make up for the non-uniform reactivity of each domain structure in the support. For the first time, nano-XAFS imaging succeeded in visualizing and identifying the modes of heterogeneous reaction and the active parts in individual catalyst particles for the oxygen storage/release process in solid–solutions. This promising technique may provide deeper insight and understanding of heterogeneous catalysis and allow development of new practical catalytic systems.

Experimental Section

Sample preparation: Pt (7.7 mg; Alfa Aesar) was impregnated with CZ (66.4 mg) in CH_3CN (2 mL), and the solvent was evaporated. The obtained sample (3 mg) was added to ethanol (10 mL) and mixed by ultrasonic treatment for 30 min. The suspension (4 μL) was dropped onto a SiN membrane (NTT-AT; 2 mm × 2 mm × 100 nm) with Pt grids (5 μm width, 100 μm interval) and the membrane was dried in air. The process was repeated 10 times, and the obtained membrane was calcined at 573 K for 30 min. The oxygen storage/release reactions of the membrane were performed in an XAFS cell with a flow of O_2 or 10 % H_2/N_2 at 1000 mL min^{-1} (Supporting Information, Section 11).

Characterization: The dispersion of sample particles on the SiN membrane was characterized by SEM analysis (JEOL JSM-6701F field emission SEM with BEI mode, 5.0 kV). XRD (Rigaku MultiFlex-STe, Cu $K\alpha$, 40 kV, 50 mA) was measured under air, and the (440) diffraction peak ($2\theta = 47.7$–$48.8°$) was used for the attribution of CZ phases.

Scanning nano-XRF and nano-XAFS were measured at the BL36XU and BL39XU beamlines at SPring-8, Japan. X-rays from an undulator were monochromatized by Si(111) crystals and focused by Kirkpatrick–Baez mirrors to a size of 409 (h) × 154 (v) nm (6 keV). The sample enclosed in an XAFS cell with a He flow was mounted on an encoded-feedback translation stage (10 nm resolution) at the focal point of the X-ray beam, inclined at a tilt of 30° with respect to the optical path. Incident and fluorescent X-rays were detected by a He-filled ion chamber and a 21-element Ge detector (Canberra, EGPX 40 × 40 × 7-21PIX), respectively. Scanning nano-XRF mappings were measured every 150 nm at the 122 energies around the Ce L_{III}-edge (5.68–5.80 keV). In addition to Ce $L\alpha$ fluorescent X-rays, Pt $L\alpha$ fluorescent X-rays were also detected using higher order light. Analysis of the obtained imaging data was performed by the reported method.[9] Oxygen composition was estimated by linear combination fitting of the Ce L_{III}-edge nano-XANES spectra of pyrochlore $Ce_2Zr_2O_7$ and κ-phase $Ce_2Zr_2O_8$.

Acknowledgements

The authors thank Dr. Y. Nagai (Toyota Central R&D Labs. Inc.). We also thank Dr. S. Nakao (IMS) for SEM measurements and N. Takada (IMS) for sample preparation. XAFS measurements were performed with the approval of SPring-8 proposals (2011B1889, 2013B7821, 2014A7821, 2014B7821, and 2015A7821). This work was supported in part by the NEXT program (GR090), the NEDO program, JSPS KAKENHI Grant-in-Aid for Scientific Research (B) (26288005), JSPS KAKENHI Grant-in-Aid for Young Scientists (B) (16K18288), and the Murata Science Foundation.

Keywords: ceria–zirconia · heterogeneous catalysis · oxygen storage capacity · structure–activity relationships · XAFS imaging

How to cite: *Angew. Chem. Int. Ed.* **2016**, *55*, 12022–12025
Angew. Chem. **2016**, *128*, 12201–12204

[1] S. Mitchell, N. L. Michels, J. Pérez-Ramírez, *Chem. Soc. Rev.* **2013**, *42*, 6094.
[2] a) H. C. Yao, Y. F. Yu Yao, *J. Catal.* **1984**, *86*, 254; b) J. Kašpar, P. Fornasiero, M. Graziani, *Catal. Today* **1999**, *50*, 285; c) S. Matsumoto, *Catal. Today* **2004**, *90*, 183.
[3] A. Suda, Y. Ukyo, H. Sobukawa, M. Sugiura, *J. Ceram. Soc. Jpn.* **2002**, *110*, 126.
[4] a) T. Tanabe, A. Suda, C. Descorme, D. Duprez, H. Shinjoh, M. Sugiura, *Stud. Surf. Sci. Catal.* **2001**, *138*, 135; b) P. Fornasiero, J. Kašpar, V. Sergo, M. Graziani, *J. Catal.* **1999**, *182*, 56.
[5] T. Yamamoto, A. Suzuki, Y. Nagai, T. Tanabe, F. Dong, Y. Inada, M. Nomura, M. Tada, Y. Iwasawa, *Angew. Chem. Int. Ed.* **2007**, *46*, 9253; *Angew. Chem.* **2007**, *119*, 9413.
[6] a) M. Tada, S. Zhang, S. Malwadkar, N. Ishiguro, J. Soga, Y. Nagai, K. Tezuka, H. Imoto, S. O.-Y. Matsuo, S. Ohkoshi, Y. Iwasawa, *Angew. Chem. Int. Ed.* **2012**, *51*, 9361; *Angew. Chem.* **2012**, *124*, 9495; b) M. Tada, N. Ishiguro, T. Uruga, H. Tanida, Y. Terada, S. Nagamatsu, Y. Iwasawa, S. Ohkoshi, *Phys. Chem. Chem. Phys.* **2011**, *13*, 14910.
[7] a) I. L. C. Buurmans, B. M. Weckhuysen, *Nat. Chem.* **2012**, *4*, 873; b) B. M. Weckhuysen, *Angew. Chem. Int. Ed.* **2009**, *48*, 4910; *Angew. Chem.* **2009**, *121*, 5008.
[8] a) S. Kalirai, U. Boesenberg, G. Falkenberg, F. Meirer, B. M. Weckhuysen, *ChemCatChem* **2015**, *7*, 3674; b) F. Meirer, D. T. Morris, S. Kalirai, Y. Liu, J. C. Andrews, B. M. Weckhuysen, *J. Am. Chem. Soc.* **2015**, *137*, 102; c) S. Takao, O. Sekizawa, S. Nagamatsu, T. Kaneko, T. Yamamoto, G. Samjeské, K. Higashi, K. Nagasawa, T. Tsuji, M. Suzuki, N. Kawamura, M. Mizumaki, T. Uruga, Y. Iwasawa, *Angew. Chem. Int. Ed.* **2014**, *53*, 14110; *Angew. Chem.* **2014**, *126*, 14334; d) T. Saida, O. Sekizawa, N. Ishiguro, M. Hoshino, K. Uesugi, T. Uruga, S. Ohkoshi, T. Yokoyama, M. Tada, *Angew. Chem. Int. Ed.* **2012**, *51*, 10311; *Angew. Chem.* **2012**, *124*, 10457; e) I. D. Gonzalez-Jimenez, K. Cats, T. Davidian, M. Ruitenbeek, F. Meirer, Y. Liu, J. Nelson, J. C. Andrews, P. Pianetta, F. M. F. de Groot, B. M. Weckhuysen, *Angew. Chem. Int. Ed.* **2012**, *51*, 11986; *Angew. Chem.* **2012**, *124*, 12152.
[9] N. Ishiguro, T. Uruga, O. Sekizawa, T. Tsuji, M. Suzuki, N. Kawamura, M. Mizumaki, K. Nitta, T. Yokoyama, M. Tada, *ChemPhysChem* **2014**, *15*, 1563.
[10] P. Fornasiero, G. Balducci, R. Di Monte, J. Kašpar, V. Sergo, G. Gubitosa, A. Ferrero, M. Graziani, *J. Catal.* **1996**, *164*, 173.
[11] T. Omata, H. Kishimoto, S. Otsuka-Yao-Matsuo, N. Ohtori, N. Umesaki, *J. Solid State Chem.* **1999**, *147*, 573.
[12] a) J. El Fallah, S. Boujana, H. Dexpert, A. Kiennemann, J. Majerus, O. Touret, F. Villain, F. Le Normand, *J. Phys. Chem.* **1994**, *98*, 5522; b) D. R. Modeshia, C. S. Wright, J. L. Payne, G. Sankar, S. G. Fiddy, R. I. Walton, *J. Phys. Chem. C* **2007**, *111*, 14035.
[13] G. N. Vayssilov, Y. Lykhach, A. Migani, T. Staudt, G. P. Petrova, N. Tsud, T. Skála, A. Briux, F. Illas, K. C. Prince, V. Matolin, K. M. Neyman, J. Libuda, *Nat. Mater.* **2011**, *10*, 310.

Received: June 21, 2016
Revised: July 27, 2016
Published online: August 30, 2016

